Energy & Environmental Science

ROYAL SOCIETY OF CHEMISTRY

PAPER

View Article Online
View Journal | View Issue

Cite this: *Energy Environ. Sci.*, 2026, **19**, 1565

TiO_2-coated rutile oxide catalysts for acidic oxygen evolution: a design principle

Georgios K. Stavroglou, Adrian M. Frandsen, Henrik H. Kristoffersen, Katrine L. Svane and Jan Rossmeisl *

Green hydrogen production through water electrolysis under acidic conditions is limited by the efficiency of the anodic oxygen evolution reaction (OER). In this study, we outline a design principle for developing active and potentially stable rutile oxide electrocatalysts for acidic OER. Using density functional theory, we find that the adsorption energies for Ti, Sn, and Zr active sites correlate with the position of the Fermi level relative to the oxygen 2s states as the surrounding oxide composition is varied. This trend is not observed for platinum-group elements. We attribute this difference to the inability of Ti, Sn, and Zr active sites to access oxidation states above the 4+ of the rutile structure, according to changes in geometry and charge. Ti emerges as an adsorption site of special interest, since varying the composition of the surrounding rutile oxide allows titanium sites to reach theoretical overpotentials as low as 0.14 V. We then demonstrate tunable activity for TiO_2-coated conductive rutile substrates. Based on literature evidence that TiO_2 coatings improve stability under acidic OER conditions without substantially compromising activity, we suggest that a TiO_2 overlayer can serve as both an active site and corrosion protection. We propose a composition-based model that successfully finds Ir and Ru free compositions ($W_xPt_{1-x}O_2$, $W_{0.46}Pd_{0.54}O_2$) that can activate the applied TiO_2 overlayer.

Received 15th December 2025,
Accepted 21st January 2026

DOI: 10.1039/d5ee07605f

rsc.li/ees

Broader context

Proton-exchange membrane water electrolysers offer significant advantages over alkaline water electrolysers in the production of green hydrogen, including higher current densities, a high-purity hydrogen gas and a compact device design. As catalysts for the anodic oxygen evolution reaction (OER), oxides based on Ir offer the best compromise between activity and stability, however, the scarcity of Ir limits the industrial scalability of this technology. Earth-abundant alternatives are usually either active but unstable under acidic conditions, or stable but not sufficiently active. This work outlines a design principle for the fabrication of active and stable TiO_2-coated rutile oxide catalysts for the acidic OER. Our calculations demonstrate that the activity of a Ti site correlates with the position of the Fermi level of the surrounding oxide. By choosing the right surrounding oxide composition, Ti sites can be activated to achieve low OER overpotential. The same principle is found to apply for TiO_2 overlayer(s) which can then act as both active site and corrosion protection. The Fermi level energy of the host oxide can be predicted based on the composition, making it possible to construct Ir- and Ru-free catalysts with predicted high OER activity.

Introduction

Practical strategies for storing electricity from renewable energy sources, *e.g.* in the form of chemical fuels, are crucial to reduce dependence on fossil fuels. Molecular hydrogen is a suitable fuel in this context, since it can be efficiently generated through water electrolysis (WE).[1] Alkaline WE is a well-established technology relying on transition metal based catalysts,[2,3] however proton exchange membrane water electrolysis (PEMWE), which operates under acidic conditions, offers several advantages over the alkaline setup, including higher current densities, purer product gas and more compact devices.[4] The oxygen evolution reaction (OER), occurring at the anode, is recognised as the kinetic bottleneck in both alkaline and acidic water electrolysis.[5] The limitation arises because the OER consists of four proton-coupled electron transfer steps, *e.g.* for the conventionally assumed adsorbate evolution mechanism (AEM, see Section S1 in the SI for illustration):

$$* + H_2O(l) \rightarrow *OH + H^+ + e^- \quad (1)$$

$$\Delta G_1 = \Delta G_{*OH} - eU_{RHE}$$

$$*OH \rightarrow *O + H^+ + e^- \quad (2)$$

$$\Delta G_2 = \Delta G_{*O} - \Delta G_{*OH} - eU_{RHE}$$

Center for High Entropy Alloy Catalysis (CHEAC), Department of Chemistry, University of Copenhagen, Universitetsparken 5, 2100 Copenhagen, Denmark. E-mail: jan.rossmeisl@chem.ku.dk

$$*O + H_2O(l) \rightarrow *OOH + H^+ + e^- \quad (3)$$

$$\Delta G_3 = \Delta G_{*OOH} - \Delta G_{*O} - eU_{RHE}$$

$$*OOH \rightarrow * + O_2(g) + H^+ + e^- \quad (4)$$

$$\Delta G_4 = \Delta G_{O_2} - \Delta G_{*OOH} - eU_{RHE}$$

where * denotes the active site and U_{RHE} is the potential of the electrode relative to the reversible hydrogen electrode (RHE). Ideally, the free energy of all four steps (ΔG_1, ΔG_2, ΔG_3, and ΔG_4) should be equal to the thermodynamic potential of 1.23 V, but in practice the universal scaling relations relate the adsorption free energies of *OH and *OOH ($\Delta G_{*OOH} \approx \Delta G_{*OH} + 3.2$ eV), which implies that a minimum potential of 1.6 V must be applied for all steps to have a negative free energy.[6,7]

Within this limitation, oxides based on Ir and Ru are the most efficient catalysts for acidic OER.[8–14] IrO_2 is less active than RuO_2, but IrO_2 is substantially more stable.[8,10] Both IrO_2 and RuO_2 are metallic conductors,[15] facilitating electron transport in the anode catalyst and offering low electronic resistance. However, the low abundance of Ir and Ru precludes industrial upscaling of this technology.[16] Materials based on earth-abundant elements are usually either stable but inert or active but unstable under acidic OER conditions. Research on catalysts based on earth-abundant elements has therefore often followed one of two approaches: activating stable materials or stabilising active materials.[17,18]

Stable materials that are based on low-cost elements have been doped to enhance their OER activity. For example, TiO_2 is stable in acid,[19] but it is a poor OER catalyst because it is a semiconductor.[20] Both experimental and theoretical studies have demonstrated that the catalytic activity can be enhanced by doping.[21–24] The dopant introduces new states in the band gap, which determine the Fermi level. In particular, introducing one or two subsurface layers of $SrRuO_3$ into inert $SrTiO_3$ enhanced the experimentally measured OER activity under alkaline conditions, which was attributed to new electronic states introduced by the dopant.[25] In a later computational study, this concept was extended by introducing a single subsurface layer of different transition metals into $SrTiO_3$, $SrZrO_3$, TiO_2, and ZrO_2, and a correlation between the Fermi level and catalytic activity was established.[26] Since the catalytic activity is influenced by the energy position of the dopant states in the band gap, it is desirable to be able to tune these states, which is difficult to achieve with a single dopant. Co-doping with both n-type (electron-donor) and p-type (electron-acceptor) dopants has therefore been investigated, demonstrating that the OER activity of TiO_2 and $SrTiO_3$ can be tuned.[20,21] As an extreme case of the co-doping strategy, Ti atoms incorporated in a conducting high-entropy oxide (HEO), *i.e.* an oxide containing five different metals, were theoretically predicted to be highly active.[27]

Protecting active but unstable catalysts by coating or enriching them with a stable oxide such as TiO_2 is an alternative strategy for improving catalyst performance. Dimensionally stable anodes (DSAs), used in the commercial production of chlorine, employ this strategy.[28] DSAs consist of a mixture of active precious-metal oxides such as RuO_2 and IrO_2, together with TiO_2, which offers stability. Such mixtures have therefore been extensively studied, and it has been shown that the formation of an ultrathin TiO_2 coating on oxide nanoparticles consisting of Ru, Ti, and Nb resulted in improved stability during chlorine evolution.[29] Thin TiO_2 coatings have also been formed on active catalysts such as MnO_2 and Co_3O_4, resulting in improved stability without significant loss of activity.[30,31] Such coatings can be readily made by atomic layer deposition (ALD),[30,32] thermal diffusion,[29] sputter deposition,[31] and electrodeposition.[33]

The catalytic activity for OER on oxides can be estimated computationally by calculating the free energies of the individual steps along the reaction pathway (eqn (1)–(4)). Correlations between catalytic activity and the adsorption energies of reaction intermediates are often represented by volcano plots.[34,35] In particular, ΔG_2 has been proposed as a universal descriptor of OER activity.[7] It is attractive to relate these adsorption energies to electronic properties of the material to provide an understanding of the adsorption process and reduce the effort required to predict the catalytic activity of new materials.[36] A range of electronic descriptors have been widely studied in the literature, inspired by the success of the d-band model from Hammer and Nørskov. They showed that the binding energy on metal surfaces is linearly dependent on the energy difference between the center of the metal d-band and the Fermi level of the material.[37,38] This approach has been less successful in describing the adsorption energies on oxides. In contrast, the positions of the O_{2p} band, t_{2g} band, the occupancy of the e_g orbital, and the vacuum level relative to the Fermi level have all been identified as alternative descriptors for different systems.[22,26,39–43]

Here, guided by the fundamental ideas from these previous efforts, we outline a new design principle for developing active and potentially stable electrocatalysts for the OER under acidic conditions. We first study Ru, Rh, Ir, Os, Pd, Pt, Ti, Sn, and Zr ''guest'' atoms substituted at surface sites in rutile oxide slabs (''host'') with a range of element compositions. Using density functional theory (DFT), we show how the adsorption energies of *OH and *O intermediates on these guest sites change as the host composition, and therefore its Fermi level, is varied. For Ti, Sn, and Zr guests, the adsorption energies show a pronounced variation that correlates with the host Fermi level, whereas Ru, Rh, Pd, Pt, Os, and Ir guests show only low variations, which are independent of the Fermi level. By studying changes in the geometry and the charge at the adsorption site, we show that this difference is related to the inability of the Ti, Sn, and Zr guest elements to access oxidation states higher than the 4+ oxidation state of the rutile structure. Ti is particularly interesting, as it spans binding energies corresponding to OER overpotentials as low as 0.14 V. Motivated by this, we further extend the concept from single Ti sites to TiO_2 overlayers applied as coatings on conductive rutile oxides (substrates). The overpotentials on TiO_2 overlayers coating

substrates of various compositions showed trends similar to those for single Ti sites. Finally, we show that a simple linear model can successfully predict the Fermi level of the TiO_2-coated system from the composition of the underlying substrate oxide. Thus, substrate oxides with a Fermi level that optimally activates the TiO_2 overlayer for the OER can be designed from combinations of metal oxides that are not necessarily active or stable by themselves, making it possible to avoid Ru and Ir entirely. As an example, our model accurately predicts $W_xPt_{1-x}O_2$ and $W_{0.46}Pd_{0.54}O_2$ substrate compositions that, when coated with TiO_2, exhibit calculated OER overpotentials as low as 0.39 V.

Methodology

DFT (*cf.* Section S2 in the SI for computational details) is used to calculate the adsorption energies of the reaction intermediates *OH, *O + Hb, *O, *OOH, *O_2 + Hb, and O_2(g) + Hb, where Hb is a hydrogen atom adsorbed on a bridging oxygen atom adjacent to the adsorption site (*). These calculations are carried out for a range of adsorption site elements (guests) and surrounding oxide compositions (hosts), as illustrated in Fig. 1a. More specifically, Ru, Rh, Ir, Os, Pd, Pt, Ti, Sn, and Zr have been considered as guests, while both pure oxides of these elements (except for ZrO_2, which does not have a rutile polymorph),[44,45] and high entropy oxides have been employed as hosts. More details and structural illustrations of this dataset are provided in Sections S2 and S4 of the SI.

We focus on the (110) surfaces of rutile structures because RuO_2, IrO_2, RhO_2, OsO_2, PdO_2, PtO_2, SnO_2, and TiO_2 are all known to form a rutile polymorph.[15,46,47] Rutile is the preferred crystal structure for TiO_2,[48] RuO_2, IrO_2, OsO_2,[49] and SnO_2,[50] under standard conditions. PtO_2 prefers a distorted rutile structure,[51] rutile RhO_2 is possibly only a high-pressure phase,[52] while PdO_2 appears to have been synthesised by only one group and is unstable under standard conditions.[47] The (110) surface is the rutile facet that preserves the highest coordination number for surface atoms, and for TiO_2 it is calculated to have the lowest surface energy.[53] Furthermore, corrosion measurements on RuO_2 single crystals[54] and IrO_2 crystalline films[55] demonstrate low dissolution rates from the (110) facets, which indicate increased stability compared to other facets.

In our analysis, we included previously published adsorption energies for *O and *OH on the rutile (110) surface of near-equimolar HEOs consisting of Ru, Ti, Ir, Os and Rh (details about the HEOs dataset are provided in Sections S3 and S4 in the SI).[27] Similar HEOs in the IrOsPdPtRu, IrOsPtRhRu,

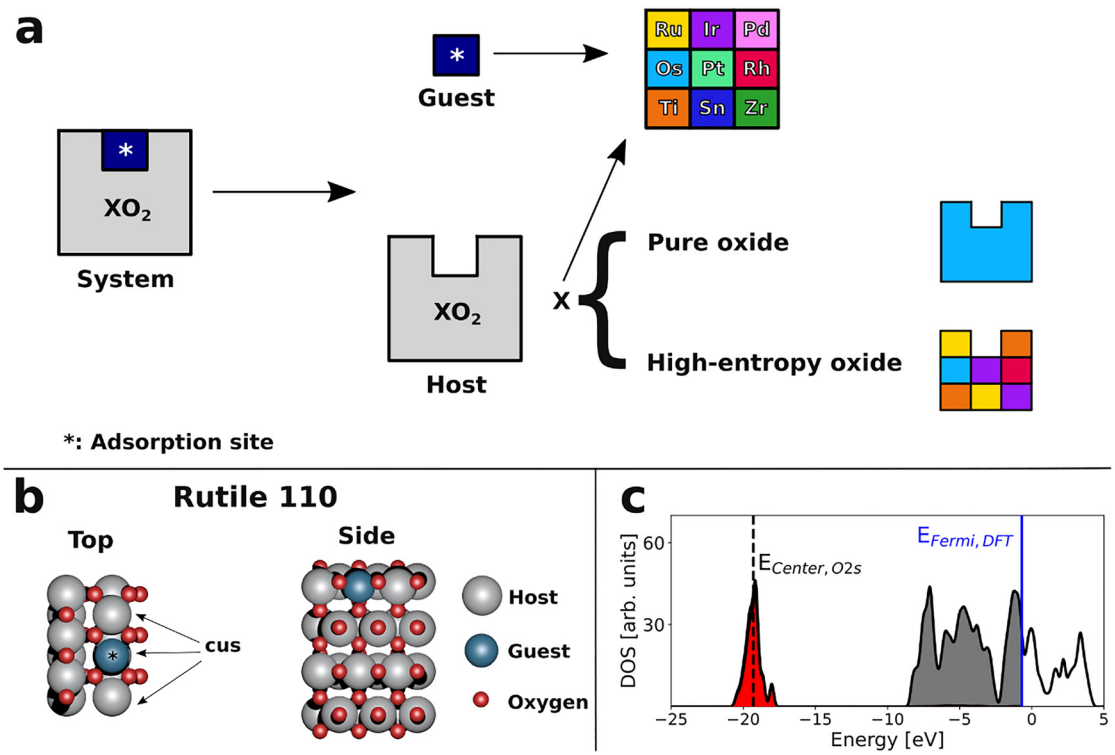

Fig. 1 (a) Schematic representation of the host–guest data, illustrating the two parts of the structure; the element of the adsorption site (guest) and the composition of the surroundings (host). Ru, Rh, Ir, Os, Pd, Pt, Ti, Sn, and Zr were studied as guests. For the host compositions, pure rutile oxides of these elements (except for ZrO_2) along with high entropy oxides were examined. (b) Top and side view of the rutile (110) surface model utilised in this study. (c) Illustration of of the Fermi level calculated by DFT ($E_{Fermi,DFT}$), relative to the oxygen 2s band on the DOS of pure RuO_2. The blue line corresponds to the $E_{Fermi,DFT}$, the red peak corresponds to the projected DOS of the oxygen 2s band of the oxygen atoms, and the black dashed line corresponds to the centroid of this band ($E_{center,O2s}$). Occupied levels are shaded.

AuOsPdPtRu, and AuIrOsPdPtReRhRu composition spaces have been prepared as nanoparticles using microwave solvothermal synthesis, and their OER activities were studied under acidic conditions.[56]

The surface model (Fig. 1b) consists of three coordinatively unsaturated sites (cus). One of these is the adsorption site and the other two are either bare or occupied with a pre-adsorbed oxygen, depending on the O* affinity of the adsorbing metal element (details are provided in Section S2 in the SI).

The adsorption free energies of the catalytic intermediates ($\Delta G_{\text{intermediate}}$) are calculated as:

$$\Delta G_{\text{intermediate}} = \Delta E_{\text{DFT}} + \Delta\text{ZPE} - T\Delta S \quad (5)$$

where ΔE_{DFT} is the DFT calculated adsorption energy (computational details are provided in Section S2 in the SI), ΔZPE and $T\Delta S$ account for changes in zero-point energy and entropy upon adsorption, respectively, and are taken from ref. 6. From the adsorption free energies, we can then calculate ΔG_1, ΔG_2, ΔG_3, and ΔG_4 at $U_{\text{RHE}} = 0$ V and employ the computational hydrogen electrode (CHE)[35] to evaluate the overpotential, η:[57]

$$\eta = \frac{\max\{\Delta G_1, \Delta G_2, \Delta G_3, \Delta G_4\}}{e} - 1.23\ \text{V} \quad (6)$$

η represents the additional potential beyond the thermodynamic 1.23 V that is required to make all four reaction steps thermodynamically downhill ($\Delta G_i \leq 0$). We plot $-\eta$ such that higher positions on the volcano correspond to lower overpotentials (higher activity).

As a descriptor for the adsorption free energies, we investigate the Fermi level, which was previously observed to correlate with the adsorption energies of OER intermediates for doped $SrTiO_3$ and TiO_2.[26] In that study, the vacuum level was used as a reference to compare DFT-calculated Fermi levels ($E_{\text{Fermi,DFT}}$) across different oxides; here, we adopt the approach in ref. 58, where $E_{\text{Fermi,DFT}}$ values are aligned using a sharp low-energy peak in the density of states (DOS) as a reference. In our case the oxygen 2s band centroid ($E_{\text{center,O2s}}$) is used as the reference point, because it is common to systems studied, lies at relatively low energies (approximately −18 eV), and generally exhibits a sharp, non-interacting peak as illustrated in Fig. 1c for RuO_2 (see Section S5 in the SI for the DOS of all pure oxides studied). In the case of RuO_2, the $E_{\text{Fermi,DFT}}$ relative to the oxygen 2s band center is 18.6 eV ($E_{\text{Fermi,RuO}_2}$) and we use this value to normalise the Fermi level energies of all systems in this study

$$E_{\text{Fermi}} = [E_{\text{Fermi,DFT}} - E_{\text{center,O2s}}] - E_{\text{Fermi,RuO}_2} \quad (7)$$

All the E_{Fermi} are calculated on the bare surface of each structure.

In addition to the host–guest dataset described above, we studied TiO_2 overlayers applied as coatings on conductive rutile oxides (substrates). We modelled pure RuO_2, RhO_2, IrO_2, OsO_2, PdO_2, and PtO_2 substrates, as well as substrates containing 89%, 78%, and 56% of each oxide, with the remainder being a random mixture of the other five oxides. To study the effect of increasing the coating thickness, the substrate oxides were investigated with both one and two TiO_2 overlayers. We also studied TiO_2-coated rutiles of $W_xPt_{1-x}O_2$ (W = tungsten, x = 0.04, 0.08, 0.12, 0.17, 0.21, and WO_2) and $W_{0.46}Pd_{0.54}O_2$, as Ir and Ru free OER candidates. For each $W_xPt_{1-x}O_2$ composition, we construct two distinct rutile slabs covered with one TiO_2 overlayer and calculate adsorption energies at all six Ti cus sites. The lattice constants of all TiO_2-coated doped structures were set to the composition weighted averages of the lattice parameters of the constituent pure oxides. More details on the TiO_2-coated dataset are provided in Sections S2 and S4 of the SI.

GGA functionals such as RPBE are known to over-delocalise electrons and to underestimate band gaps. To assess how this affects our E_{Fermi} descriptor and the band gaps of the systems in our study, we benchmarked the E_{Fermi} (as defined in eqn (7)) and the band gaps using the HSE06 hybrid functional.[59] We perform non self-consistent calculations, which have shown good agreement with self-consistent hybrid calculations[60] and are widely used,[61–63] while avoiding the computationally too demanding self-consistent HSE06 calculations for large surface slabs.

The HSE06 E_{Fermi} values calculated for the TiO_2-coated systems are on average 0.08 eV lower than the RPBE E_{Fermi} values, although there are significant outliers (Fig. S9 in the SI). We also compared the band gaps between HSE06 and RPBE for the bare surface slabs of the pure oxides (Table S4). HSE06 band gaps remain in the metallic, near-metallic regime for RuO_2, IrO_2, OsO_2, RhO_2, and WO_2, in agreement with resistivity measurements.[15] PdO_2 is also calculated to be metallic, and ref. 64 shows that Pd doping in RuO_2 improves OER activity, suggesting that Pd incorporation is unlikely to severely diminish electronic conductivity. TiO_2 and SnO_2 show much larger HSE06 band gaps than RPBE, consistent with the known GGA underestimation on semiconductors. In Fig. S8, the RPBE band gaps of the bare surface slabs for the mixed oxides studied in this work indicate metallic or near-metallic behaviour (band gap range around 0–0.15 eV).

We also studied the D3 dispersion correction[65] in the RPBE calculations for the TiO_2-coated systems. D3 introduces an approximately constant shift of 0.25 eV in ΔG_2 but the $E_{\text{Fermi}} - \Delta G_2$ trend remains essentially unchanged (Fig. S16 in the SI).

Results and discussion

The adsorption free energies of *OH ($\Delta G_{*\text{OH}}$) and *O ($\Delta G_{*\text{O}}$) intermediates on the pure oxides as a function of the E_{Fermi} of the bare surface slabs are shown in Fig. 2a and b, demonstrating clear linear correlations. Looking at the individual guest elements in the host–guest systems, two significantly different trends in the adsorption free energies are observed (Fig. 2c–f). For Ti, Sn, and Zr guests, a notable variation in the adsorption free energies that correlates with the variation in E_{Fermi} is observed (Fig. 2c and d), indicating that the adsorption energy is primarily determined by the host composition. In contrast to this, the adsorption energies for the other guest elements (Ru, Rh, Ir, Os, Pd, Pt) span a much smaller energy range and are not correlated with E_{Fermi} (Fig. 2e and f), indicating that, in these

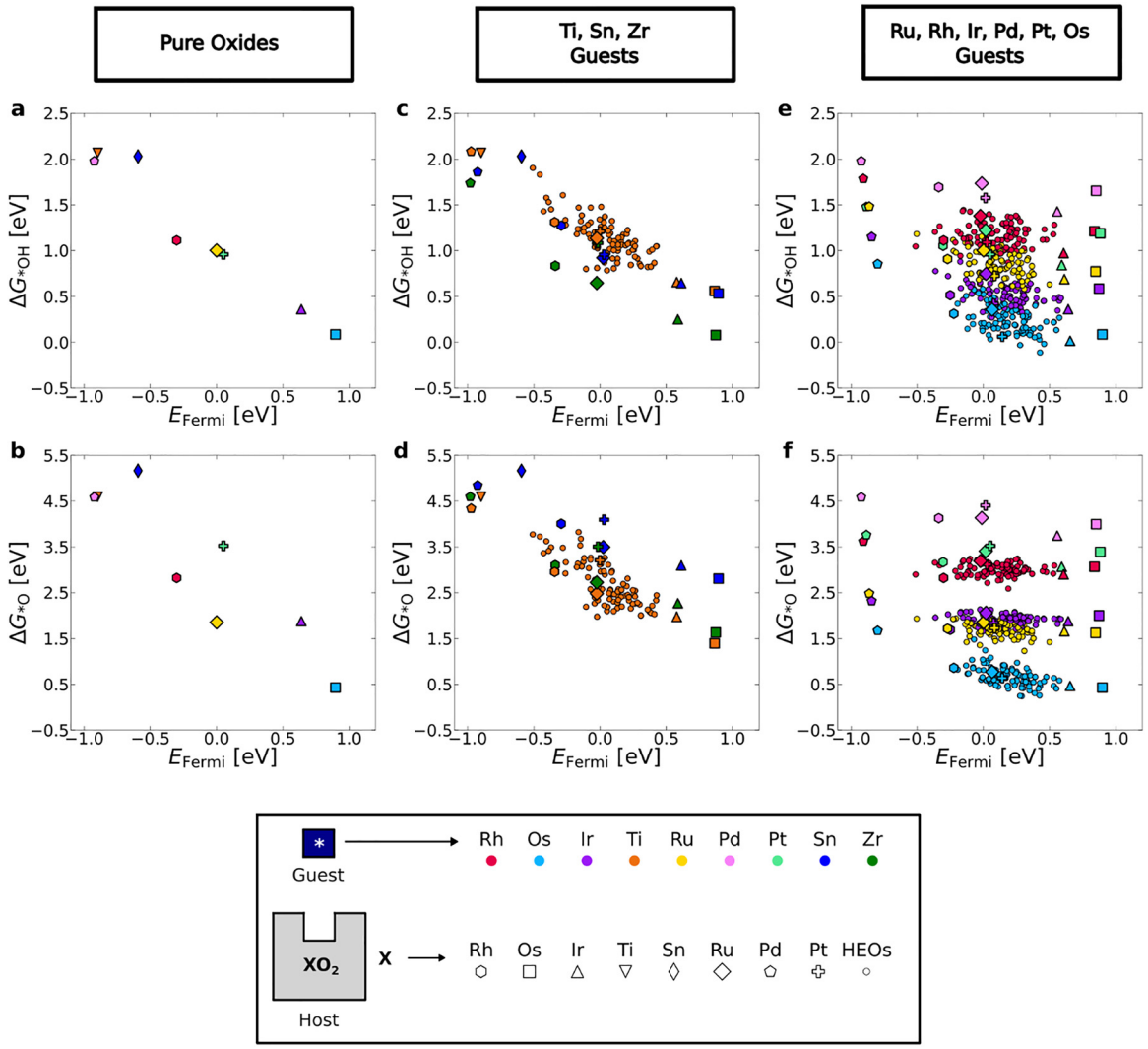

Fig. 2 Correlation between adsorption energies of the *OH and *O intermediates and the E_{Fermi} of the bare surface slabs for the pure oxides (a) and (b), the Zr, Ti, and Sn guests data (c) and (d), the Ru, Rh, Os, Ir, Pd, and Pt guests data (e) and (f). Markers represent different host compositions and colours correspond to different guest elements, as described in the legend.

systems, the adsorption energy is primarily determined by the guest element. We note that the data corresponding to SnO_2 and TiO_2 hosts are excluded from Fig. 2e and f, because their semiconducting electronic structure leads to a significantly different behaviour. Analysis of the trends in ΔG_{*O} and E_{Fermi}, as the guest element is varied for each pure-host composition (including data where TiO_2 and SnO_2 are hosts) can be found in Section S6 in the SI.

In ref. 27, a model based on the local atomic environments could predict ΔG_{*OH} and ΔG_{*O} adsorption energies. The model worked very well for Ru, Rh, Ir, and Os sites, but less well for Ti sites. We now know that *OH and *O adsorption on Ti sites depend strongly on E_{Fermi}, which was completely missing from the developed model.

To further understand the interactions between the adsorbates and the surface, we derived the scaling relation $\Delta G_{*O} = a\Delta G_{*OH} + b$, where a is the slope and b is the intercept, for each of the guest elements under study (see Section S7 in the SI). Ti, Sn, and Zr exhibit strong correlations (R^2 = 0.85–0.99) with slopes approaching 2 (a = 1.5–1.9). A relationship between OH and O adsorption energies with a slope of around 2 has been observed on metals,[66] which have multiple electrons at the Fermi level, and on oxides, except when the computational cell only contains one dopant,[67] *i.e.* when there is only one electron at the Fermi level.

To investigate the origin of the two different trends in the adsorption energies, we conducted Bader charge analysis[68] on the structures before and after the adsorption of *OH and *O. The Bader charge difference of the adsorption site atom upon adsorption of A (Δq_{*A}, A = OH or O) is calculated as the difference between the Bader charge of that atom in the bare surface (q_*) and the charge when the adsorbate is added (q_{*A}):

$$\Delta q_{*A} = q_{*A} - q_* \quad (8)$$

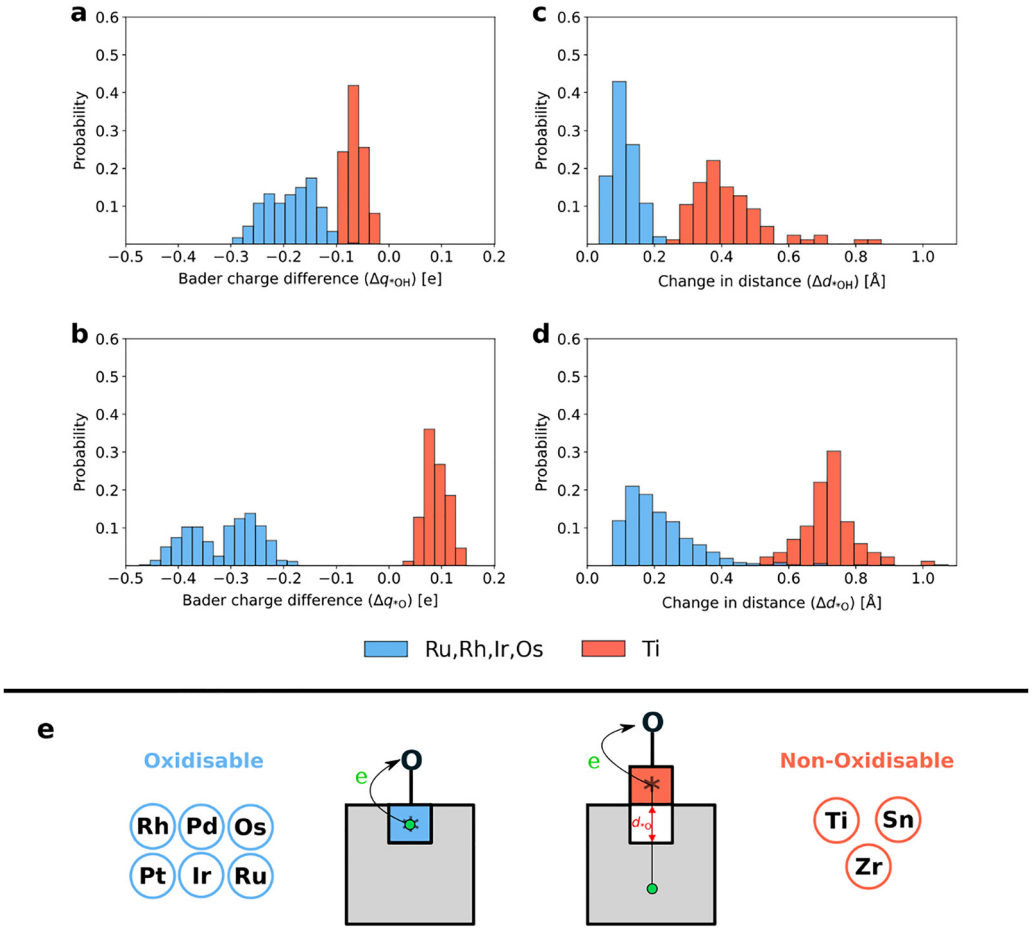

Fig. 3 Probability distributions of the Bader charge difference (Δq_{*A}) at the adsorption site atom in the RuRhIrOsTi high entropy oxides dataset after (a) *OH, and (b) *O adsorption. (c) Probability distributions of the change in the distance (Δd_{*A}) between the adsorption site atom and the oxygen atom underneath after *OH and (d) *O adsorption. Data for Ru, Rh, Ir, and Os adsorption sites are aggregated into a single distribution for comparison with the distribution based on data for Ti sites. (e) Schematic figure of the proposed explanation for the different adsorption energies trends observed for Ti, Sn, and Zr guests and Ru, Rh, Ir, Os, Pd, and Pt guests.

Using the HEO dataset, we collected the Δq_{*A} and Δq_{*O} values of Ru, Rh, Ir, and Os adsorption sites in one distribution and the corresponding values for the Ti adsorption sites in another distribution. Each set was plotted as a probability histogram, normalising each by the number of data points so that its total area equals one. The resulting plots, shown in Fig. 3a and b, demonstrate that the Ti sites exhibit a small change in charge upon OH and O adsorption. This suggests that the charge transferred to the adsorbate is supplied by the surrounding oxide rather than by the Ti adsorption site itself. This behaviour is consistent with Ti already occupying its highest oxidation state (4+) in the rutile structure. Therefore, further oxidation of the Ti site is unfavourable, and the additional charge must be supplied by the host. In contrast, Ru, Rh, Ir, and Os sites show larger changes in charge upon adsorption, indicating that electrons are, to a large extent, taken locally from the adsorption site. This is consistent with these platinum group elements being able to access oxidation states higher than 4+, making further oxidation of the metal center feasible. The trends observed for Sn, Zr, Pd and Pt adsorption sites are consistent with these conclusions, *i.e.* Sn and Zr, which also have a maximum oxidation state of 4+, behave like Ti, while Pd and Pt behave more like the other platinum group elements (see Section S8 in the SI for details).

To further elucidate the distinct trends in adsorption behaviour, we calculated the change in the distance between the adsorption site atom and the oxygen atom beneath it upon adsorption of A (Δd_{*A}, A = OH or O):

$$\Delta d_{*A} = d_{*A} - d_{*} \quad (9)$$

Again, the results for Ru, Rh, Ir, and Os are combined, while the Ti data are collected separately. The normalised distributions are shown in Fig. 3c and d, demonstrating that the Ti atoms are significantly displaced from their original position when an adsorbate is added. This observation qualitatively shows that Ti cannot form additional bonds, and to create a new bond (with the adsorbate) it therefore must weaken the bond with the oxygen atom underneath. In contrast, Ru, Rh, Ir, and Os show smaller displacement, indicating that the increased number of bonds and the associated increase in the oxidation state can be

accommodated. The observed trends for Sn, Zr, Pd, and Pt in the host–guest data generally align with these findings (see Section S9 in the SI for details). Fig. 3e summarizes that Ru, Rh, Ir, Os, Pd, and Pt sites can offer charge locally to the adsorbate, whereas Ti, Sn, and Zr sites cannot, and therefore draw charge from the surrounding oxide, while the bond between the adsorption site and the oxygen atom underneath weakens.

To evaluate the impact of the different adsorption behaviour on the OER activity, the theoretical overpotential (η) for OER has been calculated using eqn (6). We have considered both the adsorbate evolution mechanism (AEM) given in eqn (1)–(4), along with alternative pathways which have previously been studied for rutile oxides, where the proton of the *OH and *OOH intermediates is transferred to a neighbouring bridging oxygen atom to form *O + Hb and *O_2 + Hb (eqn (S1)–(S4)).[27,69–72] Additionally, we considered the pathway in which molecular oxygen desorbs from the surface already in the third step, represented as O_2(g) + Hb. Further details of the reaction pathways and illustrations of the intermediates can be found in Section S1 in the SI.

Volcano plots of the calculated theoretical overpotential based on the minimum energy pathway as a function of ΔG_2 are shown in Fig. 4. Ti, Zr, and Sn guests (Fig. 4a) exhibit a significant variation in the overpotential compared to the Ru, Rh, Ir, Os, Pd and Pt sites (Fig. 4b) in accordance with the corresponding trends in the adsorption energies. The Ti ensemble is particularly remarkable, because it includes the high-activity region near the peak of the volcano plot. Notably, many Ti sites demonstrate activities beyond the conventional volcano (as low as η = 0.14 V), due to the absence of the known scaling relation $\Delta G_{*OOH} \approx \Delta G_{*OH}$ + 3.2 eV (see Fig. S14b). In particular, O_2(g) + Hb and *O_2 +Hb intermediates are found to be thermodynamically more stable than *OOH. Meanwhile, high catalytic activity is only marginally achieved at Zr sites, and not at all at Sn sites, due to the weak binding of the *O intermediate across the entire E_{Fermi} range. Among the platinum group elements,

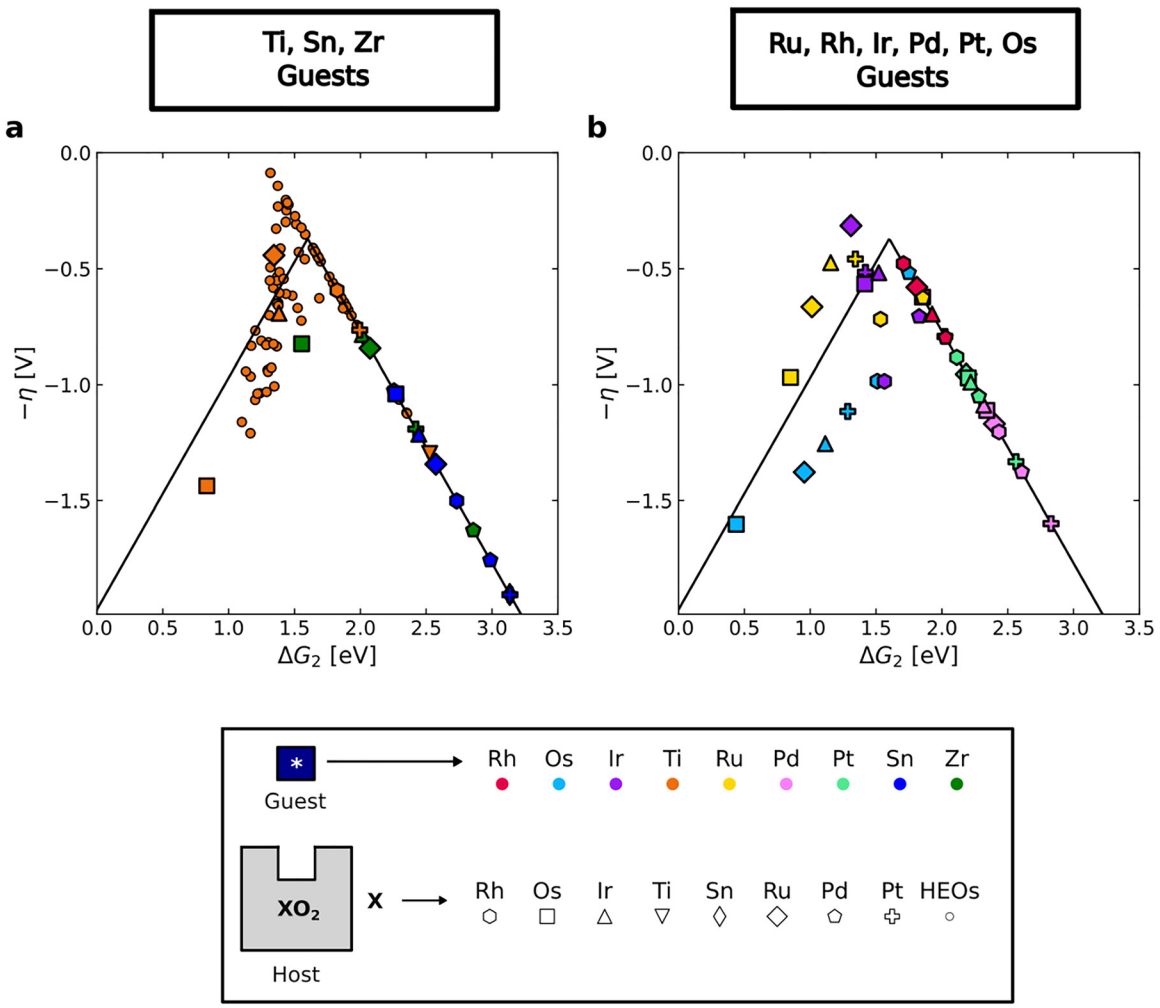

Fig. 4 Negative theoretical overpotentials ($-\eta$) of the Ti, Sn, and Zr guests (a) and the Rh, Ru, Ir, Os, Pd, and Pt guests (b) as a function of the free energy of the second catalytic step (ΔG_2) of the OER. The volcano plot line is generated by employing the known scaling relation $\Delta G_{*OOH} \approx \Delta G_{*OH}$ + 3.2 eV. Markers represent different host compositions and colours correspond to different guest elements, as described in the legend.

the Os guest data covers the widest activity range. This could be attributed to OsO_2 having the highest E_{Fermi} among the studied oxides (Fig. 2), resulting in electrons donated by Os adsorption sites having similar energies to the electrons at the E_{Fermi}.

Inspired by the tunable activity observed for Ti guest sites across different host compositions (Fig. 4a), we now extend this single-site concept to a more advantageous catalyst design by considering TiO_2 coatings on conductive rutile oxide substrates. Previous studies have shown that a TiO_2 coating can be applied on conductive oxides, often with a minor decrease in the activity and improvement of the stability under acidic OER conditions.[30–32] The feasibility of producing TiO_2 coatings of one or two monolayers is supported by ref. 29, where an ultrathin protective TiO_2 layer was formed by annealing RuO_2 nanoparticles on a Nb-doped TiO_2 support. The thickness of the TiO_2 layer was $\sim$4.4 Å, compared with $\sim$4.0 Å for a single TiO_2 monolayer. Moreover, the atomic layer deposition (ALD) technique has demonstrated exceptional control for fabricating TiO_2 coatings on IrO_2, RuO_2, and F-doped SnO_2 films.[32] In ref. 32, the average growth rate of TiO_2 was estimated *via* profilometric and scanning electron microscopy measurements to be 0.50–0.65 Å per ALD cycle. It is also possible that thicker TiO_2 coatings can be used for OER catalysis without strongly compromising activity, since ref. 30 reports that TiO_2 coatings up to 5.5 nm on Co_3O_4 increase durability without significantly affecting the activity relative to bare Co_3O_4.

To investigate whether TiO_2 coatings exhibit tunable activity, as observed for Ti guest sites, we calculated the adsorption energies and overpotentials on TiO_2-coated rutile oxides composed of the conductive elements studied above, namely Ru, Rh, Ir, Os, Pt, and Pd (see Methodology section). The ΔG_2 of these systems is plotted against the E_{Fermi} in Fig. 5a and b. A strong correlation is demonstrated ($R^2 > 0.8$), with the linear fit showing a consistent slope of around -0.8 for one TiO_2 and two TiO_2 overlayers, close to the slope obtained for the single Ti sites (-0.92). This demonstrates the robustness of the E_{Fermi} as a descriptor for the adsorption energies on both single Ti sites and TiO_2 overlayers. More details and illustrations of the slab structures in this dataset are provided in Sections S2 and S4 of the SI.

The theoretical overpotential based on the minimum energy pathway is directly compared to the E_{Fermi} for these systems in Fig. 5c and d. From these plots, it is evident that TiO_2-coated oxides can be highly active if they have a suitable E_{Fermi}. Notably, a system with a E_{Fermi} close to 0 eV (compared to the E_{Fermi} of RuO_2), can yield low overpotentials beyond the conventional volcano (Fig. 5c). The shape of these distributions suggests a volcano-type activity trend. Adding a second TiO_2 overlayer increases the overpotential (Fig. 5d), consistent with experimental observations that thicker TiO_2 coatings on Co_3O_4 progressively decrease OER performance.[30] Scaling relations of the adsorption energies and conventional volcano plots for the TiO_2-coated oxides data can be found in the Section S11 of the SI.

To further expand the use of the E_{Fermi} as a descriptor, we propose a model ($E_{Fermi,model}$) which predicts the E_{Fermi} of TiO_2-coated oxides based on the composition of the substrate oxide (excluding the TiO_2 overlayer). Specifically, this model is a weighted average of the E_{Fermi} of the pure oxides,

$$E_{Fermi,model} = \frac{1}{N_{total}} \sum_i \left(N_i \cdot E_{Fermi,i}\right) \quad (10)$$

where $E_{Fermi,i}$ is the Fermi level of the bare surface slab of the pure oxide of the element i, N_i is the number of atoms of the element i and N_{total} is the total number of the metal atoms (we do not count the oxygen atoms) in the surface slab.

In Fig. 6a, $E_{Fermi,model}$ values predicted by eqn (10) are plotted against the E_{Fermi} (calculated from eqn (7)) for the TiO_2-coated oxides with one TiO_2 overlayer. A strong correlation is observed (R^2 = 0.98 and MAE = 0.04 eV), showing that the composition of the substrate oxide is a straightforward way to engineer the E_{Fermi} of TiO_2-coated oxides. We note that while the model is clearly successful for mixtures primarily consisting of platinum-group elements, it may be too simplistic for some combinations of elements, for example, when mixing results in changes in oxidation states.

Based on the observation that the activity of TiO_2-coated rutile oxides can be tuned through the substrate oxide E_{Fermi} (Fig. 5), and that the E_{Fermi} of the TiO_2-coated systems can be predicted from the substrate oxide composition using the linear model in eqn (10) (Fig. 6a), we now apply this to predict Ir- and Ru-free OER candidates. We also exclude Rh and Os, because they are equally or even more scarce and expensive than Ru and Ir.[16] Instead, we select TiO_2-coated PtO_2 as a representative system, whose activity is not yet optimal, and dope it with tungsten (W) to tune E_{Fermi}.

In Fig. 6b, we show that the model (eqn (10)) successfully predicts the E_{Fermi} of the TiO_2-coated $W_xPt_{1-x}O_2$ data. The two distinct rutile slabs for each composition are found to have similar E_{Fermi}, indicating that E_{Fermi} is largely controlled by composition rather than the specific arrangement of metal atoms in the slab. In Fig. 6c, we see that the adsorption energies vary almost linearly with the E_{Fermi}, and the trend is shifted smoothly from the TiO_2-coated PtO_2 towards the TiO_2-coated WO_2 direction, as the amount of W increases. The observed scatter arises from an inequivalent local coordination environment associated with the distinct atomic configurations at the three different Ti-cus sites sampled on each composition. This indicates that E_{Fermi} is not a perfect descriptor, since all six adsorption sites (three Ti sites for each of the two atomic configurations) experience similar E_{Fermi}. In Fig. 6d, it is evident that these systems follow the expected volcano trend. The largest improvement in overpotential is observed for $W_{0.12}Pt_{0.88}O_2$ and $W_{0.17}Pt_{0.83}O_2$ (as low as 0.55 V), compared with the PtO_2 substrate composition (0.73 V), indicating that higher activity can be achieved while reducing precious-metal content. Increasing the W content further to 21 at% reduces the activity, indicating that the $W_xPt_{1-x}O_2$ substrate composition is optimal at x = 12–17 at%.

We applied the same design principle to predict active Pd-based catalysts. In Fig. 6, we show TiO_2-coated $W_{0.46}Pd_{0.54}O_2$

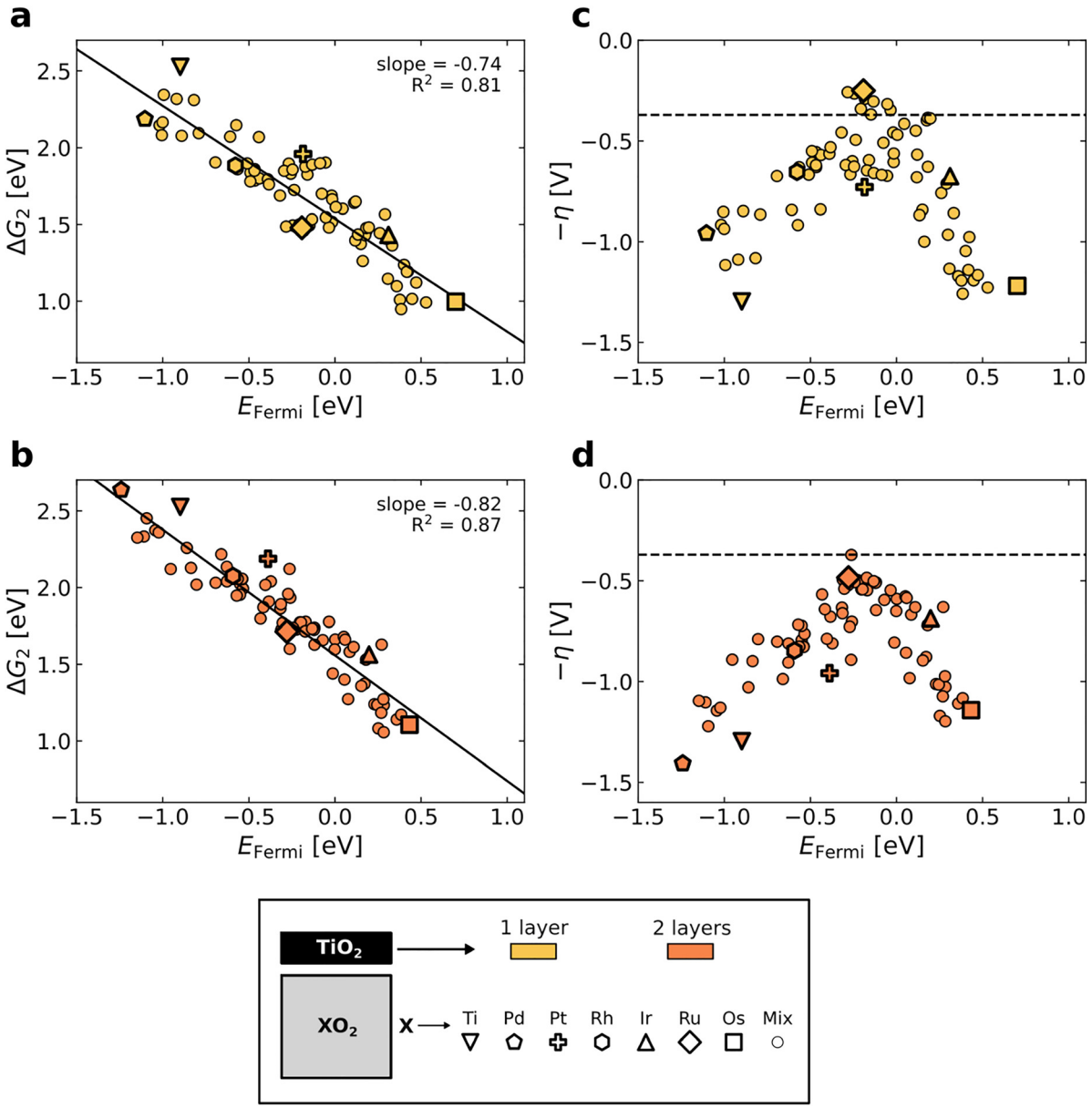

Fig. 5 Correlation between E_{Fermi} and ΔG_2 for rutile oxides coated with one overlayer (a) and two overlayers (b) of TiO_2. Black lines correspond to the best linear fits. Negative theoretical overpotentials ($-\eta$) as a function of the E_{Fermi} for the rutile oxides covered with one overlayer (c) and two overlayers (d) of TiO_2. The dashed horizontal line indicates the value of the overpotential at the apex of the activity volcano defined by the conventional scaling relation $\Delta G_{*OOH} \approx \Delta G_{*OH}$ + 3.2 eV. Markers represent different substrate oxide compositions and colours correspond to different number of TiO_2 overlayers as described in the legend.

(purple star), which has a significantly lower overpotential (η = 0.39 V) than the TiO_2-coated PdO_2 (η = 0.96 V). Together with the TiO_2-coated $W_xPt_{1-x}O_2$ results, this demonstrates that tuning the substrate E_{Fermi} provides a robust route to designing Ru and Ir free catalysts.

Conclusions

In summary, our work presents a theoretical design principle for active and potentially stable OER electrocatalysts under acidic conditions. We find that elements which cannot be oxidised beyond the 4+ oxidation state in the rutile structure (Ti, Sn, and Zr) exhibit adsorption energies and activities that are correlated with the E_{Fermi} of the surrounding oxide, whereas this behaviour is not observed for Pt, Pd, Ir, Os, Ru, and Rh sites. Among these, Ti is found to be particularly special, as it spans a wide range of adsorption energies, many of which correspond to very low overpotentials (η = 0.14 V).

We then show that these observations on single Ti sites can be transferred to a more advantageous catalyst design by

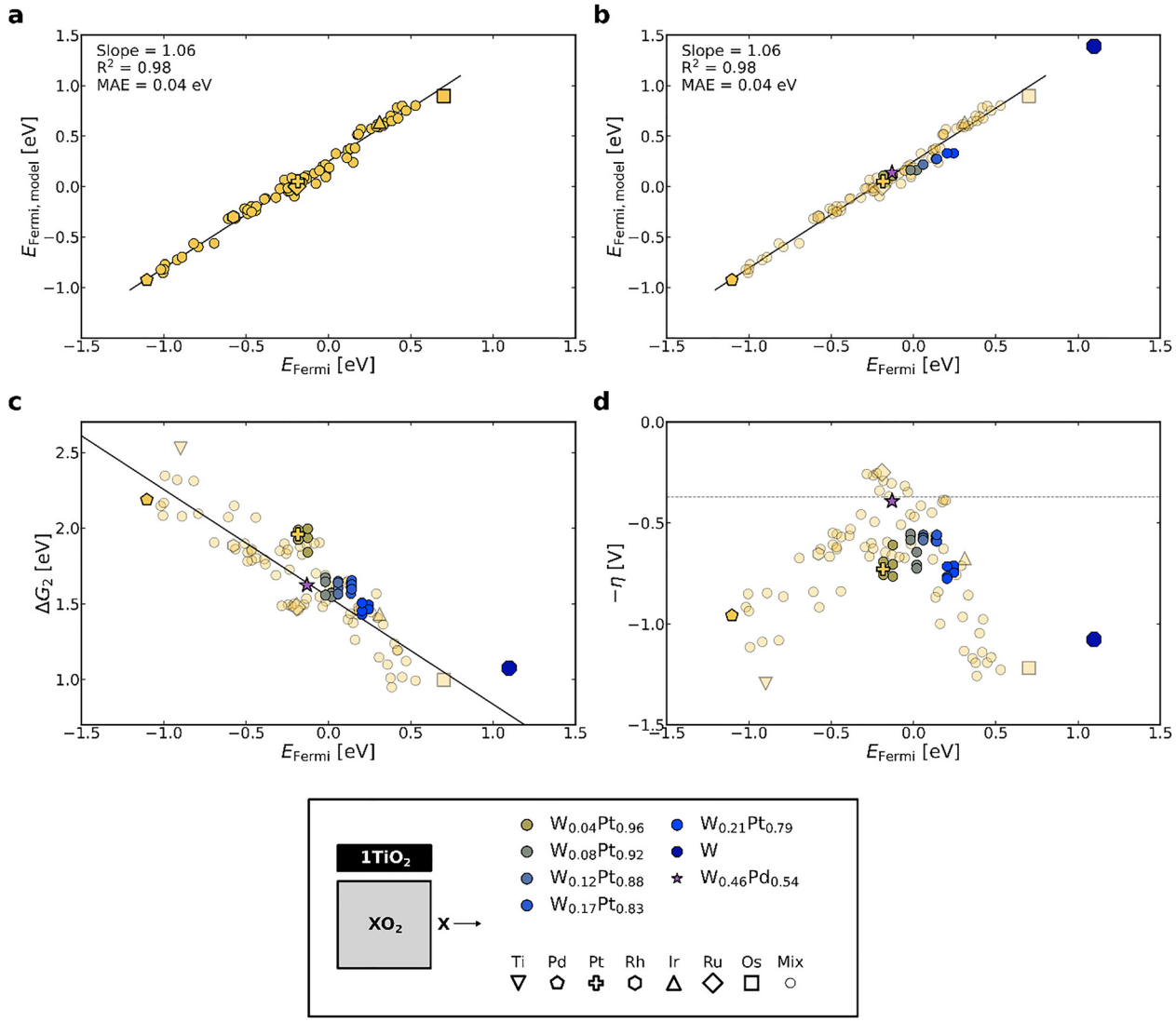

Fig. 6 (a) Correlation between the composition-based model (eqn (10)) and the real E_{Fermi} data obtained from DFT (eqn (7)) for oxides covered with one TiO_2 overlayer. The black line corresponds to the best linear fit. (b) The $W_xPt_{1-x}O_2$ and $W_{0.46}Pd_{0.54}O_2$ substrate compositions have been predicted based on the model (eqn (10)). (c) Correlation between E_{Fermi} and ΔG_2 for the $W_xPt_{1-x}O_2$ and $W_{0.46}Pd_{0.54}O_2$ substrate oxides. The semi-transparent data points and the linear fit (black line) correspond to the data shown in Fig. 5a. (d) Negative theoretical overpotentials ($-\eta$) as a function of the E_{Fermi} for the $W_xPt_{1-x}O_2$ and $W_{0.46}Pd_{0.54}O_2$ substrate oxides. The semi-transparent points correspond to the data shown in Fig. 5c. The dashed horizontal line indicates the value of the overpotential at the apex of the activity volcano defined by the conventional scaling relation $\Delta G_{*OOH} \approx \Delta G_{*OH} + 3.2$ eV.

studying TiO_2 coatings on conductive rutile oxide substrates. For these systems, a volcano-type relationship is observed between activity and E_{Fermi}, demonstrating that a TiO_2-coated oxide with a suitable E_{Fermi} can be highly active and potentially stable under acidic OER conditions, consistent with experimental reports that TiO_2 coatings can preserve activity while improving stability in acid.[19,29–32] Furthermore, we show that a simple linear model can accurately predict the E_{Fermi} of TiO_2-coated oxides based on the composition of the substrate oxide. Using this model, we identify Ir and Ru free substrate compositions, $W_xPt_{1-x}O_2$ and $W_{0.46}Pd_{0.54}O_2$, with E_{Fermi} values that can activate the TiO_2 overlayer, illustrating a practical route to designing Ir and Ru free acidic OER catalysts.

Author contributions

J. R. supervised the whole project. G. K. S. performed the DFT calculations and data analysis supervised by K. L. S., H. H. K., and J. R. G. K. S., H. H. K., and K. L. S. wrote the manuscript. All authors discussed the results, provided insights and suggestions, and helped improve the manuscript.

Conflicts of interest

The authors have submitted a patent application (European application under number EP 25387103.2) covering this work.

Data availability

The data and analysis that support the findings of this study are openly available at https://www.erda.dk/archives/f73eb5ea1d7a1897bfa54659f714b3cd/published-archive.html.

Supplementary information (SI): reaction pathways for the OER; DFT calculations setup; RuRhIrOsTi high entropy oxide dataset; description of the model structures; Fermi level alignment using O 2s band centroid; trends in ΔG_{*O} and EFermi; scaling relations between adsorption energies; Bader charge differences in pure oxide hosts; change in distance between adsorption site and oxygen atom beneath in pure oxide hosts; conventional volcano plots for TiO_2-coated metal oxides; and D3-corrections. See DOI: https://doi.org/10.1039/d5ee07605f.

Acknowledgements

We acknowledge financial support from the Danish National Research Foundation, Center for High Entropy Alloy Catalysis (CHEAC) DNRF149, the European Union under ERC Synergy grant DEMI, GA no. 101118768, and V-Sustain: The VILLUM Centre for the Science of Sustainable Fuels and Chemicals (#9455) from VILLUM FONDEN.

Notes and references

1 M. K. Singla, P. Nijhawan and A. S. Oberoi, *Environ. Sci. Pollut. Res.*, 2021, **28**, 15607–15626.
2 A. Grimaud, K. J. May, C. E. Carlton, Y. L. Lee, M. Risch, W. T. Hong, J. Zhou and Y. Shao-Horn, *Nat. Commun.*, 2013, **4**, 2439.
3 M. N. Lakhan, A. Hanan, A. Hussain, I. Ali Soomro, Y. Wang, M. Ahmed, U. Aftab, H. Sun and H. Arandiyan, *Chem. Commun.*, 2024, **60**, 5104–5135.
4 S. A. Grigoriev, V. N. Fateev, D. G. Bessarabov and P. Millet, *Int. J. Hydrogen Energy*, 2020, **45**, 26036–26058.
5 E. Fabbri and T. J. Schmidt, *ACS Catal.*, 2018, **8**, 9765–9774.
6 J. Rossmeisl, A. Logadottir and J. K. Nørskov, *Chem. Phys.*, 2005, **319**, 178–184.
7 I. C. Man, H. Y. Su, F. Calle-Vallejo, H. A. Hansen, J. I. Martínez, N. G. Inoglu, J. Kitchin, T. F. Jaramillo, J. K. Nørskov and J. Rossmeisl, *ChemCatChem*, 2011, **3**, 1159–1165.
8 N. Danilovic, R. Subbaraman, K. C. Chang, S. H. Chang, Y. J. Kang, J. Snyder, A. P. Paulikas, D. Strmcnik, Y. T. Kim, D. Myers, V. R. Stamenkovic and N. M. Markovic, *J. Phys. Chem. Lett.*, 2014, **5**, 2474–2478.
9 M. Escudero-Escribano, A. F. Pedersen, E. A. Paoli, R. Frydendal, D. Friebel, P. Malacrida, J. Rossmeisl, I. E. L. Stephens and I. Chorkendorff, *J. Phys. Chem. B*, 2018, **122**, 947–955.
10 Y. Lee, J. Suntivich, K. J. May, E. E. Perry and Y. Shao-Horn, *J. Phys. Chem. Lett.*, 2012, **3**, 399–404.
11 D. Lebedev, M. Povia, K. Waltar, P. M. Abdala, I. E. Castelli, E. Fabbri, M. V. Blanco, A. Fedorov, C. Copéret, N. Marzari and T. J. Schmidt, *Chem. Mater.*, 2017, **29**, 5182–5191.
12 D. F. Abbott, D. Lebedev, K. Waltar, M. Povia, M. Nachtegaal, E. Fabbri, C. Copéret and T. J. Schmidt, *Chem. Mater.*, 2016, **28**, 6591–6604.
13 K. A. Stoerzinger, L. Qiao, M. D. Biegalski and Y. Shao-Horn, *J. Phys. Chem. Lett.*, 2014, **5**, 1636–1641.
14 P. E. Pearce, C. Yang, A. Iadecola, J. Rodriguez-Carvajal, G. Rousse, R. Dedryvère, A. M. Abakumov, D. Giaume, M. Deschamps, J.-M. Tarascon and A. Grimaud, *Chem. Mater.*, 2019, **31**, 5845–5855.
15 D. B. Rogers, R. D. Shannon, A. W. Sleight and J. L. Gillson, *Inorg. Chem.*, 1969, **8**, 841–849.
16 P. C. K. Vesborg and T. F. Jaramillo, *RSC Adv.*, 2012, **2**, 7933–7947.
17 R. Wan, T. Yuan, L. Wang, B. Li, M. Liu and B. Zhao, *Nat. Catal.*, 2024, **7**, 1288–1304.
18 W. T. Hong, M. Risch, K. A. Stoerzinger, A. Grimaud, J. Suntivich and Y. Shao-Horn, *Energy Environ. Sci.*, 2015, **8**, 1404–1427.
19 M. Pourbaix, *Atlas of Electrochemical Equilibria in Aqueous Solutions*, National Association of Corrosion Engineers, TX, 2 edn, 1974.
20 T. Kutlusoy, S. Divanis, R. Pittkowski, R. Marina, A. M. Frandsen, K. Minhova-Macounova, R. Nebel, D. Zhao, S. F. L. Mertens, H. Hoster, P. Krtil and J. Rossmeisl, *Chem. Sci.*, 2022, **13**, 13879–13892.
21 R. K. B. Karlsson, A. Cornell and L. G. M. Pettersson, *Electrochim. Acta*, 2015, **180**, 514–527.
22 M. García-Mota, A. Vojvodic, F. Abild-Pedersen and J. K. Nørskov, *J. Phys. Chem. C*, 2012, **117**, 460–465.
23 N. Roy, Y. Sohn, K. T. Leung and D. Pradhan, *J. Phys. Chem. C*, 2014, **118**, 29499–29506.
24 D. M. Jang, I. H. Kwak, E. L. Kwon, C. S. Jung, H. S. Im, K. Park and J. Park, *J. Phys. Chem. C*, 2015, **119**, 1921–1927.
25 A. R. Akbashev, L. Zhang, J. T. Mefford, J. Park, B. Butz, H. Luftman, W. C. Chueh and A. Vojvodic, *Energy Environ. Sci.*, 2018, **11**, 1762–1769.
26 L. Zhang, A. S. Raman and A. Vojvodic, *Chem. Mater.*, 2020, **32**, 5569–5578.
27 K. L. Svane and J. Rossmeisl, *Angew. Chem.*, 2022, **61**, e202201146.
28 S. Trasatti, *Electrochim. Acta*, 2000, **45**, 2377–2385.
29 H. W. Lim, D. K. Cho, J. H. Park, S. G. Ji, Y. J. Ahn, J. Y. Kim and C. W. Lee, *ACS Catal.*, 2021, **11**, 12423–12432.
30 T. Tran-Phu, H. Chen, R. Daiyan, M. Chatti, B. Liu, R. Amal, Y. Liu, D. R. Macfarlane, A. N. Simonov and A. Tricoli, *ACS Appl. Mater. Interfaces*, 2022, **14**, 33130–33140.
31 R. Frydendal, E. A. Paoli, I. Chorkendorff, J. Rossmeisl and I. E. L. Stephens, *Adv. Energy Mater.*, 2015, **5**, 1500991.
32 C. E. Finke, S. T. Omelchenko, J. T. Jasper, M. F. Lichterman, C. G. Read, N. S. Lewis and M. R. Hoffmann, *Energy Environ. Sci.*, 2019, **12**, 358–365.
33 B. Endrődi, E. Kecsenovity, K. Rajeshwar and C. Janáky, *ACS Appl. Energy Mater.*, 2018, **1**, 851–858.

34 J. Rossmeisl, Z. W. Qu, H. Zhu, G. J. Kroes and J. K. Nørskov, *J. Electroanal. Chem.*, 2007, **607**, 83–89.
35 J. K. Nørskov, J. Rossmeisl, A. Logadottir, L. Lindqvist, J. R. Kitchin, T. Bligaard and H. Jónsson, *J. Phys. Chem. B*, 2004, **108**, 17886–17892.
36 E. Fabbri, A. Habereder, K. Waltar, R. Kötz and T. J. Schmidt, *Catal. Sci. Technol.*, 2014, **4**, 3800–3821.
37 B. Hammer and J. K. Nørskov, *Surf. Sci.*, 1995, **343**, 211–220.
38 B. Hammer and J. K. Norskov, *Nature*, 1995, **376**, 238–240.
39 S. A. Akhade and J. R. Kitchin, *J. Chem. Phys.*, 2012, **137**, 084703.
40 J. Suntivich, K. J. May, H. A. Gasteiger, J. B. Goodenough and Y. Shao-Horn, *Science*, 2011, **334**, 1383–1385.
41 Y.-L. Lee, J. Kleis, J. Rossmeisl, Y. Shao-Horn and D. Morgan, *Energy Environ. Sci.*, 2011, **4**, 3966–3970.
42 Z. Xu and J. R. Kitchin, *J. Chem. Phys.*, 2015, **142**, 104703.
43 L. Giordano, K. Akkiraju, R. Jacobs, D. Vivona, D. Morgan and Y. Shao-Horn, *Acc. Chem. Res.*, 2022, **55**, 298–308.
44 G. Jomard, T. Petit, A. Pasturel, L. Magaud, G. Kresse and J. Hafner, *Phys. Rev. B: Condens. Matter Mater. Phys.*, 1999, **59**, 4044–4052.
45 Y. Han and J. Zhu, *Top. Catal.*, 2013, **56**, 1525–1541.
46 S. F. Matar, G. Demazeau, M. H. Möller and R. Pöttgen, *Chem. Phys. Lett.*, 2011, **508**, 215–218.
47 I. Shaplygin, G. Aparnikov and V. Lazarev, *Russ. J. Inorg. Chem.*, 1978, **23**, 488.
48 A. A. Levchenko, G. Li, J. Boerio-Goates, B. F. Woodfield and A. Navrotsky, *Chem. Mater.*, 2006, **18**, 6324–6332.
49 H. S. C. O'Neill and J. Nell, *Geochim. Cosmochim. Acta*, 1997, **61**, 5279–5293.
50 L. Gracia, A. Beltrán and J. Andrés, *J. Phys. Chem. B*, 2007, **111**, 6479–6485.
51 R. K. Nomiyama, M. J. Piotrowski and J. L. F. Da Silva, *Phys. Rev. B: Condens. Matter Mater. Phys.*, 2011, **84**, 100101(R).
52 R. D. Shannon, *Solid State Commun.*, 1968, **6**, 139–143.
53 H. Perron, C. Domain, J. Roques, R. Drot, E. Simoni and H. Catalette, *Theor. Chem. Acc.*, 2007, **117**, 565–574.
54 C. Roy, R. R. Rao, K. A. Stoerzinger, J. Hwang, J. Rossmeisl, I. Chorkendorff, Y. Shao-Horn and I. E. L. Stephens, *ACS Energy Lett.*, 2018, **3**, 2045–2051.
55 T. Weber, V. Vonk, D. Escalera-López, G. Abbondanza, A. Larsson, V. Koller, M. J. S. Abb, Z. Hegedüs, T. Bäcker, U. Lienert, G. S. Harlow, A. Stierle, S. Cherevko, E. Lundgren and H. Over, *ACS Catal.*, 2021, **11**, 12651–12660.
56 V. A. Mints, K. L. Svane, J. Rossmeisl and M. Arenz, *ACS Catal.*, 2024, **14**, 6936–6944.
57 M. Busch, N. B. Halck, U. I. Kramm, S. Siahrostami, P. Krtil and J. Rossmeisl, *Nano Energy*, 2016, **29**, 126–135.
58 H. H. Kristoffersen and H. Metiu, *J. Phys. Chem. C*, 2015, **119**, 10500–10506.
59 J. Heyd, G. E. Scuseria and M. Ernzerhof, *J. Chem. Phys.*, 2003, **118**, 8207–8215.
60 J. Paier, M. Marsman, K. Hummer, G. Kresse, I. C. Gerber and J. G. Angyan, *J. Chem. Phys.*, 2006, **124**, 154709.
61 H. Moustafa, J. J. Mortensen, J. Rossmeisl and K. W. Jacobsen, *Appl. Surf. Sci.*, 2024, **649**, 159168.
62 I. E. Castelli, F. Hüser, M. Pandey, H. Li, K. S. Thygesen, B. Seger, A. Jain, K. A. Persson, G. Ceder and K. W. Jacobsen, *Adv. Energy Mater.*, 2014, **5**, 1400915.
63 I. E. Castelli, I.-C. Man, S.-G. Soriga, V. Parvulescu, N. B. Halck and J. Rossmeisl, *J. Phys. Chem. C*, 2017, **121**, 18608–18614.
64 Y. Liu, X. Hu, C. Liu, S. Zhu, K. Jiang, F. Liu and S. Zheng, *Green Energy Environ.*, 2024, **9**, 937–948.
65 S. Grimme, J. Antony, S. Ehrlich and H. Krieg, *J. Chem. Phys.*, 2010, **132**, 154104.
66 F. Abild-Pedersen, J. Greeley, F. Studt, J. Rossmeisl, T. R. Munter, P. G. Moses, E. Skúlason, T. Bligaard and J. K. Nørskov, *Phys. Rev. Lett.*, 2007, **99**, 016105.
67 S. Divanis, T. Kutlusoy, I. M. Ingmer Boye, I. C. Man and J. Rossmeisl, *Chem. Sci.*, 2020, **11**, 2943–2950.
68 G. Henkelman, A. Arnaldsson and H. Jónsson, *Comput. Mater. Sci.*, 2006, **36**, 354–360.
69 N. B. Halck, V. Petrykin, P. Krtil and J. Rossmeisl, *Phys. Chem. Chem. Phys.*, 2014, **16**, 13682–13688.
70 A. Grimaud, O. Diaz-Morales, B. Han, W. T. Hong, Y. L. Lee, L. Giordano, K. A. Stoerzinger, M. T. M. Koper and Y. Shao-Horn, *Nat. Chem.*, 2017, **9**, 457–465.
71 E. Inico, G. Di Liberto and L. Giordano, *ChemCatChem*, 2024, **16**, e202400813.
72 R. R. Rao, M. J. Kolb, N. B. Halck, A. F. Pedersen, A. Mehta, H. You, K. A. Stoerzinger, Z. Feng, H. A. Hansen, H. Zhou, L. Giordano, J. Rossmeisl, T. Vegge, I. Chorkendorff, I. E. L. Stephens and Y. Shao-Horn, *Energy Environ. Sci.*, 2017, **10**, 2626–2637.

